

Spitzer MIPS 24 and 70 μm Imaging near the South Ecliptic Pole: Maps and Source Catalogs

Kimberly S. Scott¹, Hans F. Stabenau¹, Filiberto G. Braglia², Colin Borys³, Edward L. Chapin², Mark J. Devlin¹, Gaelen Marsden², Douglas Scott², Matthew D. P. Truch¹, Elisabetta Valiante², and Marco P. Viero⁴

ABSTRACT

We have imaged an 11.5 deg^2 region of sky towards the South Ecliptic Pole (RA = $04^{\text{h}}43^{\text{m}}$, Dec = $-53^{\circ}40'$, J2000) at 24 and 70 μm with MIPS, the Multi-band Imaging Photometer for *Spitzer*. This region is coincident with a field mapped at longer wavelengths by the Balloon-borne Large Aperture Submillimeter Telescope. We discuss our data reduction and source extraction procedures. The median 1σ depths of the maps are $47 \mu\text{Jy beam}^{-1}$ at 24 μm and $4.3 \text{ mJy beam}^{-1}$ at 70 μm . At 24 μm , we identify 93 098 point sources with signal-to-noise ratio (SNR) ≥ 5 , and an additional 63 resolved galaxies; at 70 μm we identify 891 point sources with SNR ≥ 6 . From simulations, we determine a false detection rate of 1.8% (1.1%) for the 24 μm (70 μm) catalog. The 24 and 70 μm point-source catalogs are 80% complete at 230 μJy and 11 mJy, respectively. These mosaic images and source catalogs will be available to the public through the NASA/IPAC Infrared Science Archive.

Subject headings: catalogs — infrared: general — surveys

1. Introduction

Understanding the formation and evolution of galaxies is one of the foremost goals of experimental cosmology today. In the redshift range $z \simeq 1-3$, massive galaxies go through an

¹Department of Physics & Astronomy, University of Pennsylvania, 209 South 33rd Street, Philadelphia, PA 19104, USA

²Department of Physics & Astronomy, University of British Columbia, 6224 Agricultural Road, Vancouver, BC V6T 1Z1, Canada

³California Institute of Technology, 1200 East California Boulevard, Pasadena, CA 91125, USA

⁴Department of Astronomy & Astrophysics, University of Toronto, 50 St. George Street, Toronto, ON M5S 3H4, Canada

evolutionary stage characterized by high rates of star formation, much of which is obscured by dust. Over the past decade, observations at sub-millimeter (sub-mm) and millimeter (mm) wavelengths ($\lambda \sim 200 - 2000 \mu\text{m}$) have resulted in the detection of thousands of dust-obscured galaxies at high redshift (e.g. Scott et al. 2002; Borys et al. 2003; Greve et al. 2004; Laurent et al. 2005; Coppin et al. 2006; Bertoldi et al. 2007; Greve et al. 2008; Scott et al. 2008, 2010; Perera et al. 2008; Weiß et al. 2009; Dye et al. 2009; Austermann et al. 2010). Though these sub-mm/mm galaxies (hereafter SMGs) account for only a small fraction of the cosmic infrared background (Puget et al. 1996; Hauser et al. 1998; Fixsen et al. 1998) at these wavelengths (e.g. Wang et al. 2006; Scott et al. 2008, 2010; Devlin et al. 2009; Marsden et al. 2009; Pascale et al. 2009), they may contribute significantly to the cosmic star-formation activity at $z \gtrsim 2$ (Chapman et al. 2005; Aretxaga et al. 2007; Dye et al. 2008). While the most luminous sources ($L_{\text{FIR}} \gtrsim 10^{12} L_{\odot}$) are readily detectable over a large range in redshift, owing to a strong negative K -correction at these wavelengths (e.g. Blain et al. 2002), the sub-mm/mm data alone provide little insight into the physical properties and redshift distribution of these galaxies, and consequently they need to be identified in other wavebands in order to understand how SMGs fit into the general picture of galaxy evolution.

Over the years, deep complementary multi-wavelength data, particularly at radio and mid-infrared (mid-IR, $\lambda \sim 8 - 50 \mu\text{m}$) wavelengths, have proven invaluable for characterizing galaxies detected at sub-mm/mm wavelengths (e.g. Pope et al. 2006; Ashby et al. 2006; Hainline et al. 2009; Chapin et al. 2009, 2010). In this paper, we describe 24 and 70 μm observations taken with the Multiband Imaging Photometer for *Spitzer* (MIPS, Rieke et al. 2004) of a region near the South Ecliptic Pole (SEP), which was recently imaged by the Balloon-borne Large Aperture Submillimeter Telescope (BLAST, Pascale et al. 2008) at 250, 350, and 500 μm . This field has one of the lowest cirrus backgrounds at mid-IR wavelengths, with a 24 μm background of 16 MJy sr $^{-1}$ — two times lower than that of the COSMOS field and comparable to the Lockman Hole and Chandra Deep Field-South (Sanders et al. 2007). The BLAST observations have revealed ~ 200 SMGs in the 8.5 deg 2 field (Valiante et al. in prep.). The depth of these *Spitzer*/MIPS observations ($5\sigma = 250 \mu\text{Jy beam}^{-1}$ at 24 μm) will allow the identification of mid-IR counterparts for $\sim 50\%$ of the BLAST-identified sources out to $z \sim 3$. These mid-IR data are also highly complementary to observations at other wavelengths already carried out towards regions within the SEP field, including: mid- and far-IR observations with *AKARI* (Matsuhara et al. 2006); mm-wavelength imaging with AzTEC on the Atacama Submillimeter Telescope Experiment (Hatsukade et al. in prep.), the South Pole Telescope, and the Atacama Cosmology Telescope; and 20-cm observations with the Australia Telescope Compact Array. A 7 deg 2 region within the SEP will also be imaged from 100-500 μm as part of the *Herschel* Multi-tiered Extragalactic Survey (HerMES)

Guaranteed Time Key Project.¹

This paper is organized as follows: In §2 we describe the 24 and 70 μm observations carried out towards the SEP field. In §3 we describe the data reduction process we use to make the 24 and 70 μm mosaic images. We discuss the source extraction and catalogs in §4, and summarize the final data products in §5.

2. Observations

The MIPS 24 and 70 μm observations of the SEP (Program ID 50581) were carried out in a single campaign (MIPS014300) from 2008 September 24-30. The astronomical observational requests (AORs) were designed to be robust against the fast rate of field rotation ($\sim 1^\circ$ per day), taking care to provide sufficient overlap to obtain complete sampling at 24 and 70 μm . The observations were taken in scan-mode using the medium scan speed ($6.5'' \text{ s}^{-1}$). We used 160'' offsets in the cross-scan direction between forward and reverse scan legs in order to achieve sufficient overlap for the 70 μm array. Each AOR consisted of nine scan legs with a length of 1.5° , and a total of 34 AORs were used to map the field to our target sensitivity ($5\sigma = 250 \mu\text{Jy beam}^{-1}$ at 24 μm). A total of 88.4 hrs was spent on these observations.

3. Mosaic Images

3.1. 24 μm Map

We start with the basic calibrated data (BCD) available from the *Spitzer* Science Center (SSC), which have been processed using version S18.1.0 of the SSC MIPS 24 μm pipeline (Gordon et al. 2005; Masci et al. 2005; Engelbracht et al. 2007). The total number of BCDs from all of the AORs is 66 093; we exclude 298 frames with unusually high noise — where the 1σ root-mean-square (rms) noise is $> 10 \text{ MJy sr}^{-1}$ — and we use the remaining 65 795 (99.5%) to make the mosaic. We combine the frames into a single mosaic image using the SSC MOsaicing and Point-source EXtraction (MOPEX) software. Before co-adding and combining the BCDs, it is necessary to perform background matching between overlapping frames in order to achieve a common background level. Given the large number of BCDs, we were unable to use the MOPEX Overlap pipeline for background matching. Instead, we

¹<http://hermes.sussex.ac.uk>

subtract the mode computed for each frame individually from the original BCDs in order to remove the background prior to mosaicing.

We use the MOPEX Mosaic pipeline (version 18.3.3) to interpolate the BCDs onto a common grid, detect and reject outliers, and co-add them into a single image. The frames are first interpolated onto a common grid in RA-Dec (J2000, tangential projection) with $2.45''$ pixels, using the default interpolation scheme. We then perform multi-frame outlier detection, which identifies and masks both moving objects and cosmic ray strikes. For each pixel in the interpolated grid, the mean and standard deviation of all pixel values from the individual frames are computed, and samples that are 5σ positive or negative outliers are masked. The frames are then re-interpolated using these masks, and these images are co-added and combined into a single mosaic image.

This initial $24\ \mu\text{m}$ mosaic image showed noticeable dark latent artifacts oriented in the scan direction over the entire field. Such low-level dark stripes are often seen in $24\ \mu\text{m}$ scan-mode maps and arise from a 1-2% reduction in the detector response when the telescope scans over a bright source. With timescales lasting longer than the length of a single AOR, these dark latent artifacts are stable and can be removed by self-calibration. Using the original BCDs, we generate an improved flat-field correction by dividing each frame by the normalized median of all of the BCDs. These represent corrections of $< 2.7\%$. The flat-fielded BCDs are then processed in the same way as the original BCDs, resulting in a mosaic image where the dark stripes are largely reduced.

The $24\ \mu\text{m}$ mosaic image of the SEP is shown in Figure 1. The map is in units of MJy sr^{-1} . The MOPEX Mosaic pipeline also produces a corresponding uncertainty map (in MJy sr^{-1}) and a coverage map (number of BCDs averaged for each pixel). However, by studying the pixel flux distribution of the mosaic image (shown in Figure 2 by the solid light-gray histogram), we find that the values in the uncertainty image overestimate the 1σ noise, as previously noted by other groups (e.g. Sanders et al. 2007). Since the uncertainty values are used in §4.1 to determine the photometry errors on extracted sources, we apply a correction factor to the uncertainty map produced by the Mosaic pipeline. We construct a realization of the noise in the mosaic map by producing a difference image of overlapping BCDs, alternatively multiplying each successive frame by ± 1 before co-adding. The flux distribution for this “jackknifed” map is shown as the black histogram in Figure 2. This technique removes the astronomical signal (both bright and confused sources) from the mosaic image while preserving the properties of the underlying noise. We next generate several simulated noise maps from the uncertainty image, assuming that the noise in each pixel is Gaussian distributed with σ equal to the pixel value in the uncertainty map. The flux distribution averaged over these noise maps is shown by the gray dotted curve in Figure 2.

We fit the flux distributions of the jackknifed noise realization and the simulated noise maps assuming Gaussian distributions; the ratio of the best-fit σ from the jackknifed map flux distribution to that of the average flux distribution from the simulated noise maps is 0.68. We scale the values in the uncertainty map produced by the Mosaic pipeline by this factor for use in source extraction and all other analyses involving the $24\ \mu\text{m}$ map.

The total area of the SEP $24\ \mu\text{m}$ map is $11.8\ \text{deg}^2$, centered at $(\text{RA}, \text{Dec}) = (04^{\text{h}}43^{\text{m}}25.6^{\text{s}}, -53^{\circ}36'41'')$. Due to the overlap of the AORs used to map the full region, the coverage in the mosaic image is non-uniform, as demonstrated in Figure 3. The median 1σ depth² is $47\ \mu\text{Jy beam}^{-1}$ and ranges from $31\text{--}110\ \mu\text{Jy beam}^{-1}$ over the inner $10\ \text{deg}^2$. Assuming a confusion limit (one source per 30 beams) of $\sim 200\ \mu\text{Jy}$, estimated from the $24\ \mu\text{m}$ number counts derived in Papovich et al. (2004) and Sanders et al. (2007), confusion effects on the map properties should be small, but non-negligible.

The spacecraft astrometry is reported to be known to better than $1.4''$. We check for a systematic shift in the astrometry by stacking the $24\ \mu\text{m}$ map at the positions of 65 stars located within the field (all of which are detected at $24\ \mu\text{m}$).³ We find that the offset is consistent with zero, and the stacked signal is well described by the $24\ \mu\text{m}$ point response function (PRF) convolved with a Gaussian with $\sigma = 1.4''$. This demonstrates that there are no systematic issues with the astrometry, and the pointing rms errors are as expected.

3.2. $70\ \mu\text{m}$ Map

For the $70\ \mu\text{m}$ data, we start with the time-filtered BCD products (fBCDs, total of 66 098) provided by the SSC, for which the majority of the data artifacts caused by variation of the residuals in the slow response and latent artifacts from stimulator flashes have already been removed. We are left with a total of 63 168 (95.6%) fBCDs after excluding those with rms noise $> 10\ \text{MJy sr}^{-1}$. As with the $24\ \mu\text{m}$ data, we remove the background prior to mosaicing by subtracting the mode from each of the frames, and we use the MOPEX Mosaic pipeline to combine the frames into a single mosaic image. We interpolate the fBCDs onto a grid with $4.0''$ pixels (the native pixel scale), and we carry out multi-frame outlier detection as described above for the $24\ \mu\text{m}$ data, masking samples that are 3σ outliers (default values in MOPEX for $70\ \mu\text{m}$ data) to produce an initial mosaic image.

²We use a conversion factor of $1530\ (\mu\text{Jy beam}^{-1})(\text{MJy sr}^{-1})^{-1}$, determined by integrating over the $24\ \mu\text{m}$ point response function (PRF) provided by the SSC.

³From the Smithsonian Astrophysical Observatory (SAO) Star Catalog: <http://heasarc.gsfc.nasa.gov/W3Browse/star-catalog/sao.html>.

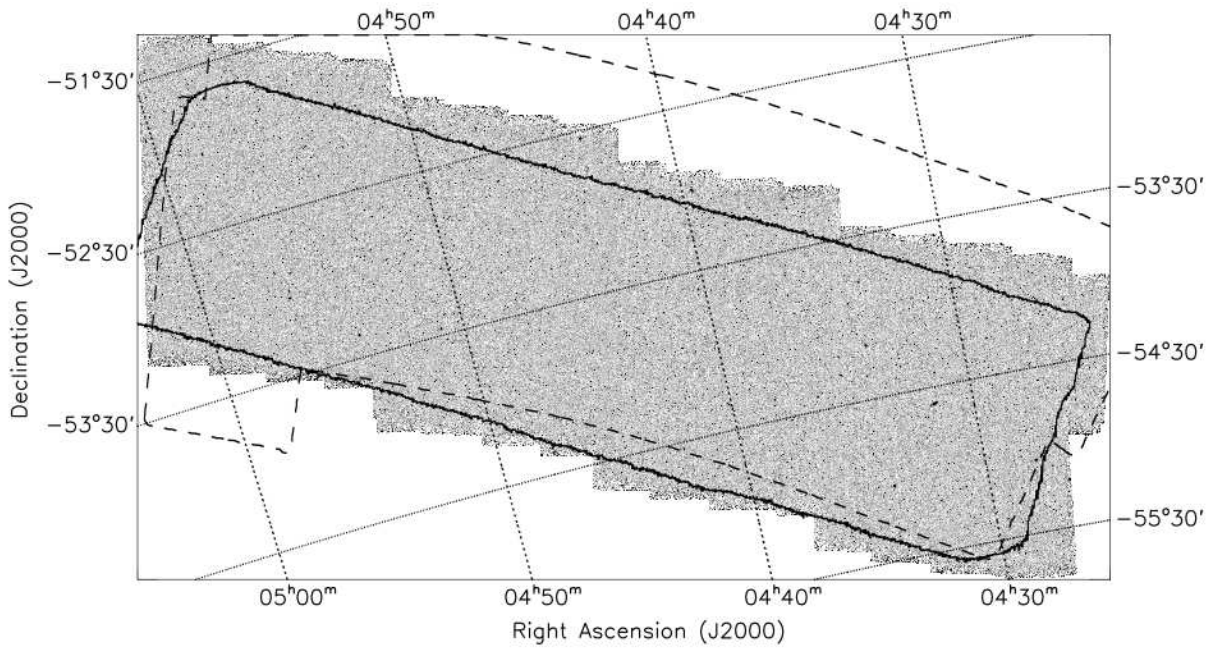


Fig. 1.— The $24\ \mu\text{m}$ mosaic image of the SEP field. The map is shown on a linear scale ranging from -0.09 to $0.3\ \text{MJy sr}^{-1}$ (roughly -3σ to 10σ). The solid contour shows the overlapping coverage in the $8.5\ \text{deg}^2$ BLAST survey of this field, while the dashed contour indicates the region mapped at $90\ \mu\text{m}$ by *AKARI*.

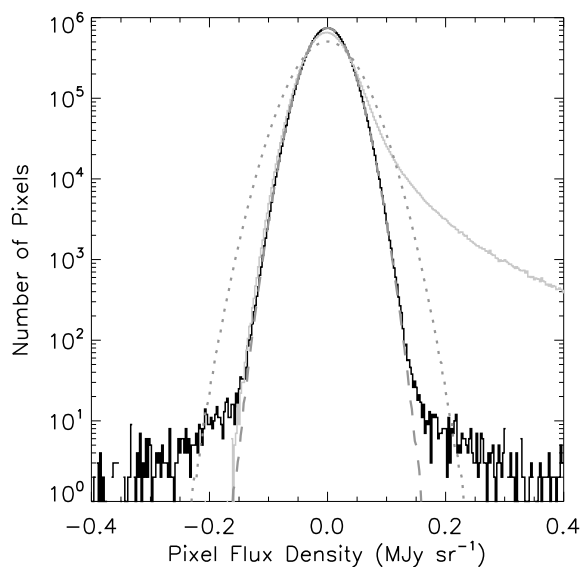


Fig. 2.— Distribution of pixel flux densities in the $24\ \mu\text{m}$ maps. The solid light-gray histogram shows the flux distribution in the mosaic map. The black histogram shows the flux distribution in the jackknifed noise map. The dotted gray curve is the average flux distribution from simulated noise maps using the original uncertainty values determined from MOPEX, and the dashed gray curve shows this distribution after applying a correction factor of 0.68.

Even with the temporal high-pass filter, “stimflash latents”, which are correlated by column, are not fully removed. To improve the $70\ \mu\text{m}$ image, we use a median column filter on the data (Frayer et al. 2006a), starting from the original BCDs and utilizing the Germanium Reprocessing Tools (GERT) available from the SSC. This column filter introduces negative side-lobes near bright sources, so we redo the filtering in two steps: 1) starting with the initial mosaic made from the fBCDs we identify the brightest 10% of sources in the map using the Astronomical Point-Source Extractor (APEX) software; 2) we then use the GERT to column filter the original BCDs with these sources masked. After this we perform a background subtraction and use the MOPEX Mosaic pipeline on these re-filtered BCDs to combine them into a single image as described in the previous paragraph.

The $70\ \mu\text{m}$ mosaic map is shown in Figure 4. As with the $24\ \mu\text{m}$ mosaic, the corresponding uncertainty image does not provide a good estimate of the 1σ uncertainty in the map; in this case it significantly underestimates the noise (see Figure 5). We use the same jackknifing technique as described in §3.1 to produce a noise realization for the $70\ \mu\text{m}$ data, and we determine a correction factor of 2.55 by comparing the flux distribution of the jackknifed map to that of simulated noise maps made from the original uncertainty image. We use this scaled uncertainty map for all analyses involving the $70\ \mu\text{m}$ data.

The total area of the $70\ \mu\text{m}$ mosaic map of the SEP is $11.5\ \text{deg}^2$, centered at (RA, Dec) = $(04^{\text{h}}43^{\text{m}}34.6^{\text{s}}, -53^{\circ}48'42'')$. The noise distribution is shown in Figure 6. The median 1σ depth⁴ is $4.3\ \text{mJy beam}^{-1}$, ranging from 2.2 to $40\ \text{mJy beam}^{-1}$ over the inner $10\ \text{deg}^2$. Given the confusion limit of $\sim 8\ \text{mJy}$ (Frayer et al. 2006a,b, 2009), the effects of confusion on the map properties may be non-negligible.

4. Source Catalogs

4.1. $24\ \mu\text{m}$ Source Extraction

We use the Astronomical Point-Source Extractor (APEX) software within the MOPEX package to detect and extract sources from the $24\ \mu\text{m}$ mosaic and to compute aperture photometry for these sources. We use the point-source probability (PSP) image for source detection and image segmentation. The PSP image is calculated from the background-subtracted mosaic image, filtered with the point response function (PRF), and represents the probability at each pixel of having a point source above the noise. Pixels that are $\geq 5\sigma$

⁴Using a conversion factor of $12.9\ (\text{mJy beam}^{-1})(\text{MJy sr}^{-1})^{-1}$ determined by integrating over the $70\ \mu\text{m}$ PRF provided by the SSC.

from the mean are identified and grouped into contiguous pixel clusters; any cluster with > 20 pixels is run through an iterative process to determine whether to split the pixel cluster into multiple sources. The PRF is then fit to the background-subtracted mosaic image at the source centroids to estimate source fluxes and refine their positions. We allow passive deblending for sources that were split into multiple pixel clusters during image segmentation, where the PRF is simultaneously fit to the blended sources. APEX computes two types of uncertainties on the PRF-fitted fluxes. The first represents the naive uncertainty from the fit, which likely underestimates the true flux uncertainty due to correlated errors. The second is computed as the quadrature sum of the data uncertainties within a box the size of the core of the PRF. This latter quantity is used to estimate the signal-to-noise ratio (SNR) for the source candidates and generally provides a better estimate of the uncertainty.⁵

We select an initial list of source candidates with $\text{SNR} \geq 5$. For each candidate we consider the PRF fitting to be successful if the χ^2 per degree of freedom (reduced χ^2) is $\chi_r^2 \leq 3$; this is true for 97% of the sources. The vast majority of the remaining candidates represent: 1) very bright point sources, many of them known stars in the field; 2) false detections surrounding these bright sources caused by features in the PRF (e.g., the Airy ring); 3) potential bright latent artifacts in the in-scan direction above and below a bright source; 4) extended sources; and 5) false detections arising from extended sources being split into multiple pixel clusters during image segmentation. Since this is a very large field that includes a wide range of sources, it is not possible to select a single group of settings to use for image segmentation that will be optimal in all cases. For this reason we consider the cases above by visually inspecting the mosaic image at the locations of source candidates with $\chi_r^2 > 3$, and removing sources that are clearly false detections from the catalog.

Due to the settings used for image segmentation, false detections surrounding bright point sources arise outside of the first Airy ring ($> 20''$ from the peak emission). From visually inspecting the full mosaic map we identify 90 bright point sources possibly surrounded by such false detections. Of these 65 are known stars. We identify false detections as follows: 1) using the APEX Quality Assurance (QA) pipeline, we subtract from the mosaic image a model for the PRF features at $> 20''$ for each of the 90 bright sources, while retaining the center peak emission inside this radius, creating a residual image; 2) we run the same source detection and extraction algorithm as used on the mosaic image for this residual map, creating a “residual” catalog; and 3) source candidates in the original catalog that are not detected in the residual catalog are false detections and are excluded in the final $24 \mu\text{m}$ catalog. An example of how we identify false positives surrounding bright point sources is

⁵http://ssc.spitzer.caltech.edu/dataanalysis/tools/mopex/mopexusersguide/91/#_Toc253561706

given in the upper left panel of Figure 7, which shows a $24\ \mu\text{m}$ postage stamp image centered on the star SAO 233646. The small circles (diameter = $6''$) and boxes mark the positions of all “sources” initially identified using APEX, where the latter represent those identified as false positives.

We additionally flag sources that remain in the residual catalog, but may also be false detections given their proximity to a bright source. Examples of these sources — which we do *not* remove from the final catalog — are represented by double circles in the upper left panel of Figure 7. These sources fall into three categories: 1) sources that may represent bright latent artifacts located in the in-scan direction (vertical axis in Figure 7); 2) sources that may actually be part of the PRF from the nearby bright source (e.g., radially extended artifacts in the PRF from the telescope secondary mirror support, oriented $\sim 60^\circ$ from the scan direction); and 3) sources located within a $35''$ radius of the bright source (black dashed circle in Figure 7, enclosing the second Airy ring). Some of these sources may also be false detections, and most will be poorly fit due to their proximity to a bright source. We describe the identification of false detections around extended sources in §4.8.

The final $24\ \mu\text{m}$ point-source catalog is available in the electronic version of the *Astrophysical Journal Supplement Series*, and the first 15 entries are shown in Table 1. There is a total of 93 098 point sources with $\text{SNR} \geq 5$, after excluding known false detections. Extended sources are discussed in §4.8 and listed separately in Table 2. The number of sources identified in this field is consistent with that found in other surveys; accounting for the expected number of false positives from noise peaks (§4.5) and incompleteness (§4.6), the number density of sources with $24\ \mu\text{m}$ flux density $S_{24} > 300\ \mu\text{Jy}$ is $0.8\ \text{arcmin}^{-2}$, compared to $0.6\text{-}0.9\ \text{arcmin}^{-2}$ observed in other deep *Spitzer* surveys (Papovich et al. 2004; Sanders et al. 2007).

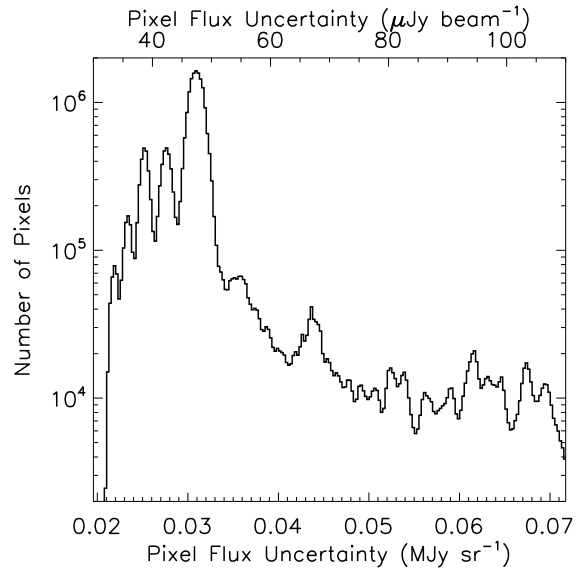


Fig. 3.— Histogram of the pixel uncertainties for the $24\mu\text{m}$ mosaic map (scaled by a factor of 0.68), demonstrating the non-uniform coverage in this map.

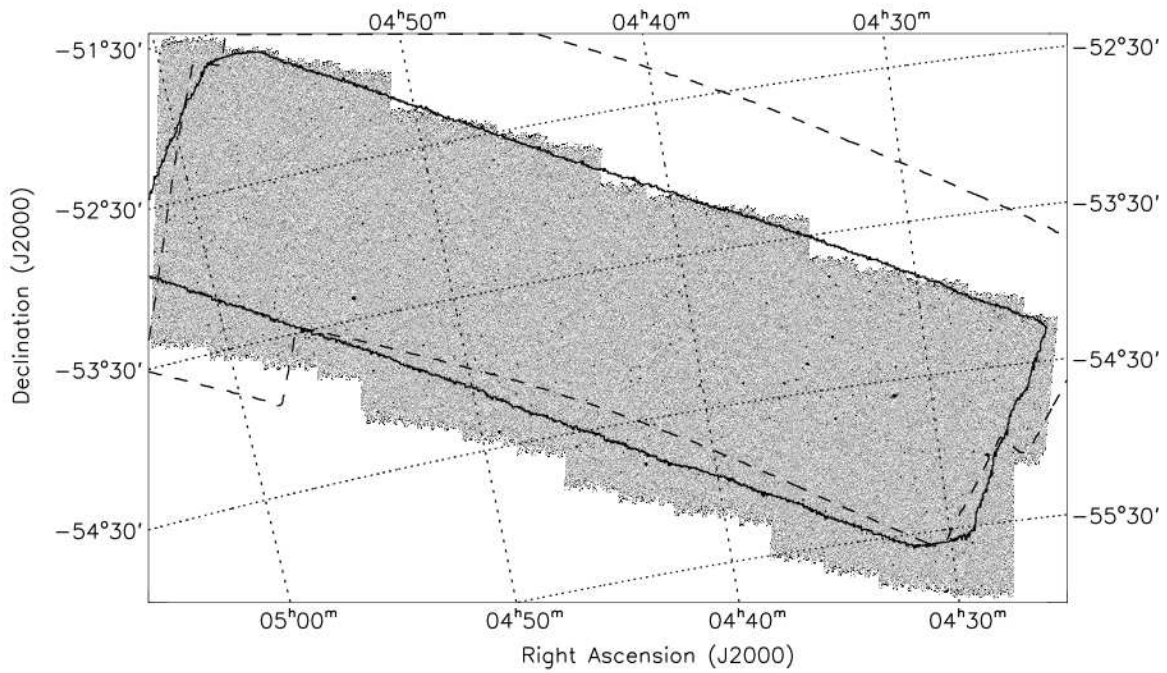


Fig. 4.— The $70\ \mu\text{m}$ mosaic image of the SEP field. The map is shown on a linear scale ranging from -0.9 to $3.0\ \text{MJysr}^{-1}$ (roughly -3σ to 10σ). The solid contour shows the overlapping coverage in the $8.5\ \text{deg}^2$ BLAST survey of this field, while the dashed contour indicates the region mapped at $90\ \mu\text{m}$ by *AKARI*.

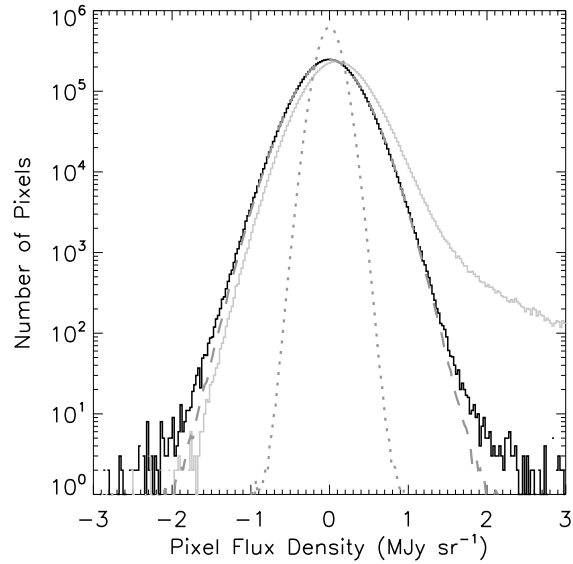


Fig. 5.— Distribution of pixel flux densities in the $70\ \mu\text{m}$ maps. The solid light-gray histogram shows the flux distribution in the mosaic map. The black histogram shows the flux distribution in the jackknifed noise map. The dotted gray curve is the average flux distribution from simulated noise maps using the original uncertainty values determined from MOPEX, and the dashed gray curve shows this distribution after applying a correction factor of 2.55.

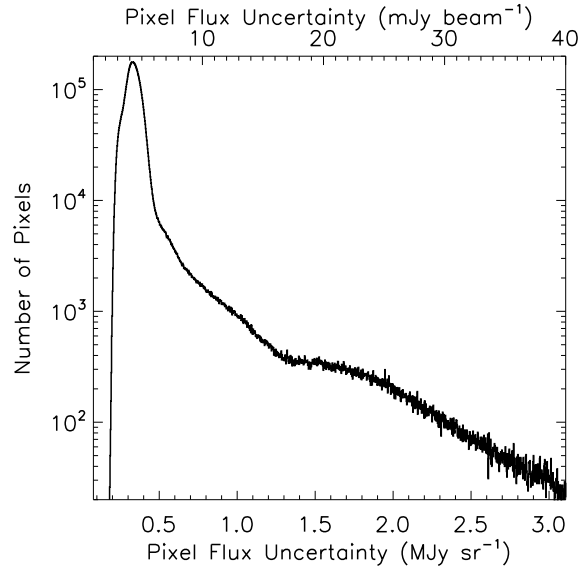


Fig. 6.— Histogram of the pixel uncertainties for the $70\ \mu\text{m}$ mosaic map (scaled by a factor of 2.55).

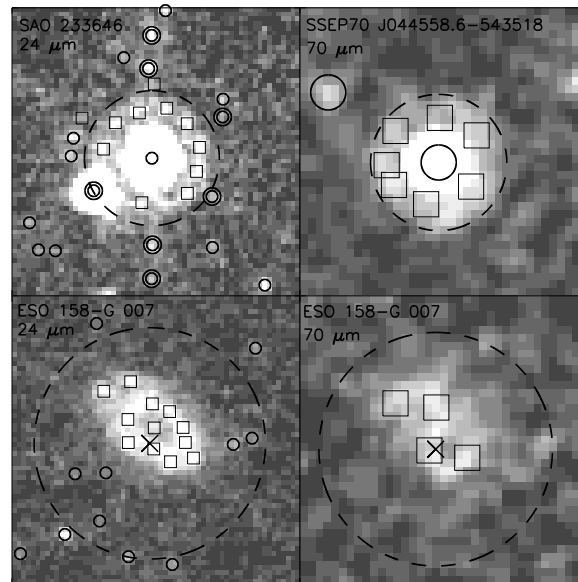


Fig. 7.— Examples of false positives surrounding bright point sources and extended sources in the $24\ \mu\text{m}$ and $70\ \mu\text{m}$ maps. All images are $2.5' \times 2.5'$ and are shown on a linear scale ranging from -0.03 to $0.3\ \text{MJy sr}^{-1}$ and -0.3 to $3.0\ \text{MJy sr}^{-1}$ for the $24\ \mu\text{m}$ and $70\ \mu\text{m}$ data, respectively. See the text for a full description of this figure.

Table 1. SEP 24 μm Point-Source Catalog

Source Name	RA (h m s J2000)	Dec ($^{\circ}$ ' " J2000)	$S_{\text{PRF}} \pm \sigma_{\text{PRF}}$ (μJy)	SNR	χ_r^2	$S_{4.9} \pm \sigma_{4.9}$ (μJy , uncorrected)	$S_{7.4} \pm \sigma_{7.4}$ (μJy , uncorrected)	$S_{15} \pm \sigma_{15}$ (μJy , uncorrected)	Comment
SSEP24 J042929.8–554314	04 29 29.87	–55 43 14.4	750 ± 57	10	1.9	394 ± 33	625 ± 52	890 ± 110	
SSEP24 J042905.9–554342	04 29 05.91	–55 43 42.9	3809 ± 55	58	1.5	1982 ± 31	2522 ± 47	3347 ± 97	
SSEP24 J042926.0–554314	04 29 26.10	–55 43 14.4	1241 ± 54	19	0.68	641 ± 30	812 ± 48	1260 ± 100	
SSEP24 J042956.6–554209	04 29 56.60	–55 42 09.6	516 ± 51	8.3	0.88	248 ± 29	208 ± 45	324 ± 92	
SSEP24 J042940.6–554228	04 29 40.64	–55 42 28.7	577 ± 45	10	0.96	291 ± 26	390 ± 40	362 ± 84	
SSEP24 J042920.4–554300	04 29 20.49	–55 43 00.3	676 ± 49	12	0.66	315 ± 27	430 ± 42	645 ± 86	
SSEP24 J042808.3–554452	04 28 08.33	–55 44 52.4	573 ± 49	9.4	1.5	275 ± 28	393 ± 44	737 ± 91	
SSEP24 J042850.8–554341	04 28 50.87	–55 43 41.1	624 ± 48	10	1.3	326 ± 28	419 ± 43	764 ± 90	
SSEP24 J043017.0–554108	04 30 17.10	–55 41 08.6	2159 ± 58	31	2.0	1135 ± 33	1579 ± 51	2700 ± 100	
SSEP24 J042828.6–554413	04 28 28.64	–55 44 13.2	490 ± 49	8.4	0.50	222 ± 27	249 ± 43	113 ± 88	
SSEP24 J042846.7–554339	04 28 46.79	–55 43 39.4	373 ± 45	6.8	2.1	148 ± 26	188 ± 40	263 ± 84	
SSEP24 J042806.9–554444	04 28 06.96	–55 44 44.3	509 ± 47	8.8	1.4	260 ± 27	398 ± 42	972 ± 85	
SSEP24 J042914.6–554247	04 29 14.63	–55 42 47.1	1720 ± 42	34	1.3	877 ± 24	1081 ± 37	1459 ± 76	
SSEP24 J042942.8–554159	04 29 42.81	–55 41 59.9	581 ± 43	11	1.0	250 ± 25	312 ± 38	449 ± 78	
SSEP24 J042829.0–554357	04 28 29.08	–55 43 57.9	542 ± 43	10	0.86	240 ± 24	259 ± 38	256 ± 79	

Note. — Table 1 is published in its entirety in the electronic edition of the *Astrophysical Journal Supplement Series*. The first 15 entries are shown here for guidance regarding its form and content. The first column gives the source name using the International Astronomical Union (IAU) format. The second and third columns list the RA and Dec for each source. The fourth column gives the PRF-fitted flux density and its formal uncertainty. The fifth column gives the SNR estimate, and the sixth column gives the reduced χ^2 for the fit. Columns 7, 8, and 9 list the (uncorrected) aperture fluxes and uncertainties (§4.7) using 4.9", 7.4", and 15" radius apertures, respectively. The last column includes comments on the sources as follows: 1) “S” - source is a known star; 2) “D” - source was passively deblended, i.e. simultaneously fit along with neighboring sources (listed consecutively in the table, having the same χ_r^2); and 3) “P” - source may actually be part of the PRF feature of a nearby bright source, a bright latent artifact, or be poorly fit due to its proximity to a bright source, as described in §4.1.

Table 2. SEP Extended Source Catalog

Source Name	RA (h m s J2000)	Dec ($^{\circ}$ ' " J2000)	$S_{24} \pm \sigma_{24}$ (mJy)	$S_{70} \pm \sigma_{70}$ (mJy)	Aperture Radius (")	Note
2MASX J04362281–5510342	04 36 22.76	–55 10 34.4	11.26 ± 0.10	112.4 ± 1.8	30	SSEP70 J043622.7–551035
2MASX J04430361–5446543	04 43 03.56	–54 46 54.2	28.03 ± 0.15	1068.0 ± 6.9	25	SSEP70 J044303.5–544652
2MASX J04453204–5434252	04 45 32.03	–54 34 25.2	5.43 ± 0.11	68.4 ± 1.7	30	SSEP70 J044531.9–543425
NGC 1602	04 27 54.97	–55 03 27.8	48.27 ± 0.28	428.2 ± 7.0^a	90	
2MASX J04314165–5455393	04 31 41.65	–54 55 39.3	3.68 ± 0.06	36.9 ± 1.2	20	SSEP70 J043141.3–545540
NGC 1596	04 27 38.11	–55 01 40.1	11.83 ± 0.38	< 24	120	
2MASX J04425888–5432544	04 42 58.86	–54 32 54.3	4.59 ± 0.06	34.9 ± 1.6	20	SSEP70 J044258.7–543257
2MASX J04451295–5427073	04 45 12.92	–54 27 06.8	7.78 ± 0.07	84.4 ± 1.6	20	SSEP70 J044513.0–542706
2MASX J04452872–5420472	04 45 28.72	–54 20 47.4	6.83 ± 0.06	107.4 ± 1.4	20	SSEP70 J044528.7–542047
2MASX J04342317–5441331	04 34 23.19	–54 41 33.0	19.23 ± 0.07	420.1 ± 3.6	20	SSEP70 J043423.1–544132
2MASX J04480892–5410540	04 48 08.91	–54 10 53.7	9.01 ± 0.07	136.0 ± 2.2	20	SSEP70 J044808.8–541054
2MASX J04354249–5435532	04 35 42.49	–54 35 53.0	5.01 ± 0.05	41.2 ± 1.1	20	SSEP70 J043542.6–543551
NGC 1617	04 31 39.53	–54 36 08.2	87.23 ± 0.41	1107.0 ± 7.7^a	135	
SUMSS J043005–543910	04 30 05.53	–54 39 10.7	2.08 ± 0.07	< 22	20	
2MASX J04284373–5438274	04 28 43.74	–54 38 27.8	5.23 ± 0.08	44.5 ± 1.4	30	SSEP70 J042843.9–543825
ESO 158–G 007	04 49 37.27	–53 54 42.5	18.59 ± 0.17	165.2 ± 3.4^a	60	
ESO 158–G 006	04 48 40.36	–53 54 43.8	15.18 ± 0.10	229.9 ± 2.2	30	SSEP70 J044840.3–535443
2MASX J04514200–5345126	04 51 42.01	–53 45 12.5	8.91 ± 0.05	126.8 ± 1.5	20	SSEP70 J045142.1–534512
ESO 157–G 047	04 39 19.13	–54 12 41.4	4.69 ± 0.15	63.2 ± 1.6	45	SSEP70 J043919.4–541238
ESO 157–G 043	04 35 15.47	–54 18 57.2	58.45 ± 0.16	720.4 ± 5.2^a	60	
IC 2085	04 31 24.24	–54 25 00.6	26.68 ± 0.23	376.2 ± 4.5^a	75	
APMUKS(BJ) B043243.73–542450.9	04 33 50.84	–54 18 40.5	4.44 ± 0.10	47.9 ± 1.5	30	SSEP70 J043350.8–541838
2MASX J04444398–5355395	04 44 43.97	–53 55 39.4	3.06 ± 0.05	27.0 ± 1.1	20	SSEP70 J044443.8–535539
2MASX J04410494–5402486	04 41 04.93	–54 02 48.6	8.51 ± 0.08	86.3 ± 1.4	25	SSEP70 J044104.8–540248
ESO 157–G 042	04 35 12.03	–54 12 20.5	11.15 ± 0.15	127.6 ± 3.2^a	60	
APMBGC 157–064–039	04 33 13.15	–54 13 57.5	4.10 ± 0.07	42.2 ± 1.2	25	SSEP70 J043312.9–541400
ESO 158–G 001	04 41 38.90	–53 54 21.4	8.81 ± 0.10	89.0 ± 1.8	30	SSEP70 J044138.9–535421
NGC 1705	04 54 13.50	–53 21 39.8	48.09 ± 0.24	1175.0 ± 6.0^a	75	
2MASX J04594242–5302365	04 59 42.41	–53 02 36.5	0.69 ± 0.06	< 20	20	
ESO 157–G 030	04 27 32.60	–54 11 48.1	7.69 ± 0.15	141.5 ± 2.0	45	SSEP70 J042732.6–541148
2MFGC 03850	04 41 52.62	–53 42 12.1	6.04 ± 0.07	80.2 ± 1.7	25	SSEP70 J044152.6–534211
2MASX J04440985–5336563	04 44 09.83	–53 36 56.5	3.01 ± 0.05	30.19 ± 0.99	20	SSEP70 J044409.8–533653
FGCE 0439	04 48 02.76	–53 26 16.4	9.85 ± 0.08	112.1 ± 1.8	25	SSEP70 J044802.6–532615
2MASX J04342117–5353522	04 34 21.20	–53 53 52.4	24.75 ± 0.08	266.9 ± 3.0	25	SSEP70 J043421.3–535352

Table 2—Continued

Source Name	RA (h m s J2000)	Dec ($^{\circ}$ ' " J2000)	$S_{24} \pm \sigma_{24}$ (mJy)	$S_{70} \pm \sigma_{70}$ (mJy)	Aperture Radius ($''$)	Note
2MASX J04263602–5406282	04 26 36.04	–54 06 28.2	14.02 ± 0.07	165.1 ± 2.2	20	SSEP70 J042636.1–540627
IC 2083	04 30 44.27	–53 58 51.0	11.68 ± 0.09	138.8 ± 1.9	25	SSEP70 J043044.0–535850
2MASX J04290665–5401202	04 29 06.67	–54 01 20.4	8.15 ± 0.07	74.2 ± 1.6	20	SSEP70 J042906.8–540120
ESO 158–G 014	04 54 45.75	–53 05 57.5	9.39 ± 0.11	150.8 ± 2.2	35	SSEP70 J045445.7–530557
2MASX J04283256–5359474	04 28 32.55	–53 59 47.5	13.03 ± 0.06	237.5 ± 3.1	20	SSEP70 J042832.4–535947
2MASX J04505562–5312459	04 50 55.61	–53 12 45.6	20.40 ± 0.13	320.0 ± 2.5^a	50	
2MASX J04334493–5346467	04 33 44.92	–53 46 46.8	73.17 ± 0.07	487.3 ± 3.5	20	SSEP70 J043344.9–534646
2MASX J04293931–5352464	04 29 39.35	–53 52 46.6	54.27 ± 0.07		20	
ESO 158–G 012	04 53 42.79	–52 58 53.6	3.89 ± 0.10	30.5 ± 1.5	30	SSEP70 J045342.8–525852
2MASX J04305049–5347492	04 30 50.50	–53 47 48.8	5.52 ± 0.07	< 163	20	
ESO 157–G 036	04 29 49.59	–53 48 52.8	1.07 ± 0.11		35	
2MFGC 04056	04 57 21.43	–52 46 59.1	3.04 ± 0.10	< 29	30	
2MASX J04530951–5254202	04 53 09.53	–52 54 20.4	17.82 ± 0.09	321.4 ± 2.7	25	SSEP70 J045309.4–525420
APMBGC 157–032–065	04 29 03.65	–53 44 51.4	2.18 ± 0.12		25	
2MASX J05003544–5232576	05 00 35.42	–52 32 57.4	2.52 ± 0.08	< 22	25	
IC 2079	04 28 30.82	–53 44 16.5	28.76 ± 0.30		45	
ESO 158–G 008	04 49 51.13	–52 59 37.4	3.36 ± 0.13	< 26	40	
2MASX J04452961–5308249	04 45 29.63	–53 08 24.8	7.42 ± 0.06	99.9 ± 1.9	20	SSEP70 J044529.8–530822
2MASX J04574760–5233553	04 57 47.60	–52 33 55.4	4.86 ± 0.07	58.3 ± 1.6	20	SSEP70 J045747.4–523354
2MASX J04540432–5242323	04 54 04.32	–52 42 32.5	4.59 ± 0.06	49.8 ± 1.4	20	SSEP70 J045404.1–524234
AM 0445–525	04 46 12.27	–52 54 48.7	4.16 ± 0.07	< 23	20	
ESO 157–IG 051	04 41 25.15	–52 59 50.4	26.24 ± 0.08	< 368	25	
ESO 157–IG 048	04 39 25.19	–53 02 57.8	8.30 ± 0.07		20	
APMUKS(BJ) B045842.18–521729.7	04 59 52.60	–52 13 07.1	3.28 ± 0.07	38.2 ± 1.4	20	SSEP70 J045952.5–521303
ESO 157–G 049	04 39 36.88	–53 00 45.5	166.90 ± 0.17		50	
2MASX J04485406–5230438	04 48 54.07	–52 30 43.5	13.43 ± 0.07	201.0 ± 2.0	20	SSEP70 J044853.9–523044
FGCE 0448	04 54 09.47	–52 11 00.7	3.92 ± 0.09	55.0 ± 1.5	25	SSEP70 J045409.6–521059
2MASX J04580461–5125420	04 58 04.62	–51 25 42.1	5.36 ± 0.07		20	
ESO 203–G 012	04 57 26.03	–51 22 49.1	13.53 ± 0.18		35	

Note. — The extended source catalog. Column 1 gives the source name from the NASA Extragalactic Database (NED). The RA and Dec are listed in columns 2 and 3. The measured 24 and 70 μm fluxes and their uncertainties are given in columns 4 and 5, respectively. The aperture radius used for the 24 μm flux is in column 6. The last column lists the 70 μm counterpart from the point-source catalog (Table 3),

where available. Upper limits (5σ) are listed for sources not in the $70\mu\text{m}$ point-source catalog. For sources with no $70\mu\text{m}$ flux listed, the source lies outside of the coverage region of that map.

^a $70\mu\text{m}$ flux measured using the aperture radius listed in column 6.

4.2. 70 μm Source Extraction

We use the APEX software to detect and extract sources from the 70 μm mosaic. Unlike the 24 μm data, we do not use the PSP image for source detection; we find that this smooths the data too much and results in a large number of false detections. Instead, image segmentation is performed on the background-subtracted image. Pixels that are $\geq 5\sigma$ from the mean are grouped into contiguous pixel clusters, and clusters with > 70 pixels are run through the iterative process to determine whether to divide them into multiple sources. As with the 24 μm sources, the background-subtracted 70 μm mosaic image is fit to the PRF at the source centroids to measure the source fluxes and positions.

All of the extracted sources have $\text{SNR} \geq 6$ (estimated from the data uncertainties as described in §4.1), however, we again note that this value cannot be directly interpreted in terms of statistical significance. We consider the PRF fitting to be successful if $\chi_r^2 \leq 3$, which is true for 93% of the sources. The remaining source candidates are primarily bright point sources surrounded by false detections arising from features in the PRF, and extended sources, which are sometimes split into multiple sources during image segmentation. The first case is demonstrated in the upper right panel of Figure 7, which shows the 70 μm postage stamp image centered on SSEP70 J044558.6-543518. Sources initially identified by APEX are indicated by the smaller circles (diameter = $18''$) and boxes, where the latter represent false positives surrounding the bright point source and are located within a $35''$ radius containing the first Airy ring. We visually inspect the full mosaic image and remove any sources that are clearly false detections from the 70 μm catalog.

The final 70 μm point-source catalog is available in the electronic version of the *Astrophysical Journal Supplement Series*, and the first 15 entries are shown in Table 3. There is a total of 891 point sources with $\text{SNR} \geq 6$, after excluding known false detections. Extended sources are listed separately in Table 2 and discussed in §4.8. The number density of 70 μm sources with flux density $S_{70} > 19 \text{ mJy}$ observed in the SEP field (80 deg^{-2}) is marginally consistent with that observed in Frayer et al. (2009, 60 deg^{-2}) and other 70 μm surveys (Frayer et al. 2006a,b).

Table 3. SEP 70 μm Point-Source Catalog

Source Name	RA (h m s J2000)	Dec ($^{\circ}$ ' " J2000)	$S_{\text{PRF}} \pm \sigma_{\text{PRF}}$ (mJy)	SNR	χ^2_{r}	$S_{16} \pm \sigma_{16}$ (mJy, uncorrected)	$S_{28} \pm \sigma_{28}$ (mJy, uncorrected)	$S_{36} \pm \sigma_{36}$ (mJy, uncorrected)	Comment
SSEP70 J042854.2–555308	04 28 54.25	–55 53 09.0	55.6 ± 1.7	34	1.3	37.0 ± 1.1	57.3 ± 1.8	70.6 ± 2.3	
SSEP70 J042820.1–555302	04 28 20.17	–55 53 02.1	57.3 ± 1.4	42	0.30	36.14 ± 0.88	50.6 ± 1.5	60.6 ± 2.0	
SSEP70 J042846.9–555102	04 28 46.95	–55 51 02.4	33.1 ± 1.5	21	0.40	21.61 ± 0.99	26.8 ± 1.7	22.3 ± 2.2	
SSEP70 J043006.1–554910	04 30 06.10	–55 49 10.1	43.9 ± 1.5	29	0.60	36.31 ± 0.98	59.2 ± 1.7	70.6 ± 2.1	D
SSEP70 J043006.2–554852	04 30 06.30	–55 48 52.3	37.8 ± 1.4	25	0.60	33.25 ± 0.93	58.4 ± 1.6	70.0 ± 2.1	D
SSEP70 J043133.4–554429	04 31 33.43	–55 44 29.4	34.1 ± 1.6	21	0.85	22.0 ± 1.1	29.6 ± 1.8	36.1 ± 2.2	
SSEP70 J043157.5–554305	04 31 57.58	–55 43 05.8	41.4 ± 1.5	26	0.83	25.1 ± 1.0	30.3 ± 1.8	37.4 ± 2.3	
SSEP70 J043246.9–554044	04 32 46.93	–55 40 44.5	105.3 ± 1.7	66	2.0	72.1 ± 1.1	102.4 ± 1.7	119.5 ± 2.1	D
SSEP70 J043248.6–554039	04 32 48.67	–55 40 39.7	18.5 ± 1.5	12	2.0	41.3 ± 1.0	88.1 ± 1.7	104.7 ± 2.2	D
SSEP70 J042812.6–554601	04 28 12.68	–55 46 01.9	27.5 ± 1.3	20	0.70	18.91 ± 0.89	23.4 ± 1.5	29.5 ± 2.0	
SSEP70 J042951.3–554404	04 29 51.39	–55 44 04.1	46.0 ± 1.7	27	0.46	29.7 ± 1.1	40.1 ± 1.9	44.5 ± 2.3	
SSEP70 J042905.9–554343	04 29 05.95	–55 43 43.5	58.4 ± 1.6	38	0.53	36.2 ± 1.0	45.1 ± 1.7	49.9 ± 2.1	
SSEP70 J043050.2–554131	04 30 50.29	–55 41 31.4	45.3 ± 1.6	29	0.40	30.8 ± 1.1	47.3 ± 1.7	55.5 ± 2.1	
SSEP70 J043347.3–553710	04 33 47.34	–55 37 10.2	26.2 ± 1.5	16	0.30	18.7 ± 1.0	29.9 ± 1.8	43.4 ± 2.3	
SSEP70 J043017.0–554111	04 30 17.05	–55 41 11.9	33.4 ± 1.4	23	0.63	21.95 ± 0.97	31.3 ± 1.6	35.8 ± 2.1	

Note. — Table 3 is published in its entirety in the electronic edition of the *Astrophysical Journal Supplement Series*. The first 15 entries are shown here for guidance regarding its form and content. The first column gives the source name in IAU format. The second and third columns list the RA and Dec for each source. The fourth column gives the PRF-fitted flux density and its formal uncertainty. The fifth column gives the SNR estimate, and the sixth column gives the reduced χ^2 for the fit. Columns 7, 8, and 9 list the (uncorrected) aperture flux densities and uncertainties (§4.7) using 16'', 28'', and 36'' radius apertures, respectively. The last column indicates sources that were passively deblended.

4.3. Point Response Function

In fitting the source candidates to estimate their flux densities and positions, we use the 24 and 70 μm PRFs available from the SSC that had been produced using the MOPEX PRF Estimate pipeline on previous data-sets.⁶ We compare these to PRFs derived from our own data. For the 24 μm data, we use the PRF Estimate pipeline to cut and co-add postage-stamp images centered on 47 of the bright stars within this field, excluding those that are close to and/or confused with other bright sources, so as to get a clean estimate of the PRF. For the 70 μm data, we estimate the PRF by co-adding postage-stamp images centered on 129 70 μm sources detected with $\text{SNR} \geq 50$ that are located far from other sources in the map and are not resolved galaxies. The radially averaged PRFs estimated from the SEP *Spitzer* data, and their angular profiles at the first Airy ring, are shown in Figure 8. We find that the PRFs estimated from our data are in good agreement (within the measurement uncertainties) with the PRFs provided by the SSC, which are shown in Figure 8 for comparison. Since the latter are less noisy, we elect to use the PRF estimates from the SSC for point-source extraction and for all other analyses described below.

4.4. Calibration and Color Corrections

The uncertainty in the absolute flux calibration of point sources is $\sim 4\%$ and $\sim 7\%$ at 24 and 70 μm , respectively (Engelbracht et al. 2007; Gordon et al. 2007). We use the default flux conversion factors from instrument units of $0.0447 \text{ MJy sr}^{-1}$ at 24 μm and 702 MJy sr^{-1} at 70 μm , which are determined from frequent observations of primary and secondary calibrator stars assuming a blackbody spectrum with $T = 10\,000 \text{ K}$. Since extragalactic sources may have a very different spectrum across the 24 and 70 μm bands, color corrections should be applied to the flux densities listed in Tables 1, 2, and 3. However, given the range in spectral energy distributions (SEDs) and redshifts expected for different types of sources, it is difficult to choose a single template that will be appropriate for all sources. For this reason, we choose not to apply color corrections to the flux density measurements, and advise users of this catalog to compute their own (or alternatively, use the color corrections listed in the MIPS Instrument Handbook for an appropriate source spectrum) when needed.

⁶<http://ssc.spitzer.caltech.edu/mips/calibrationfiles/prfs/>

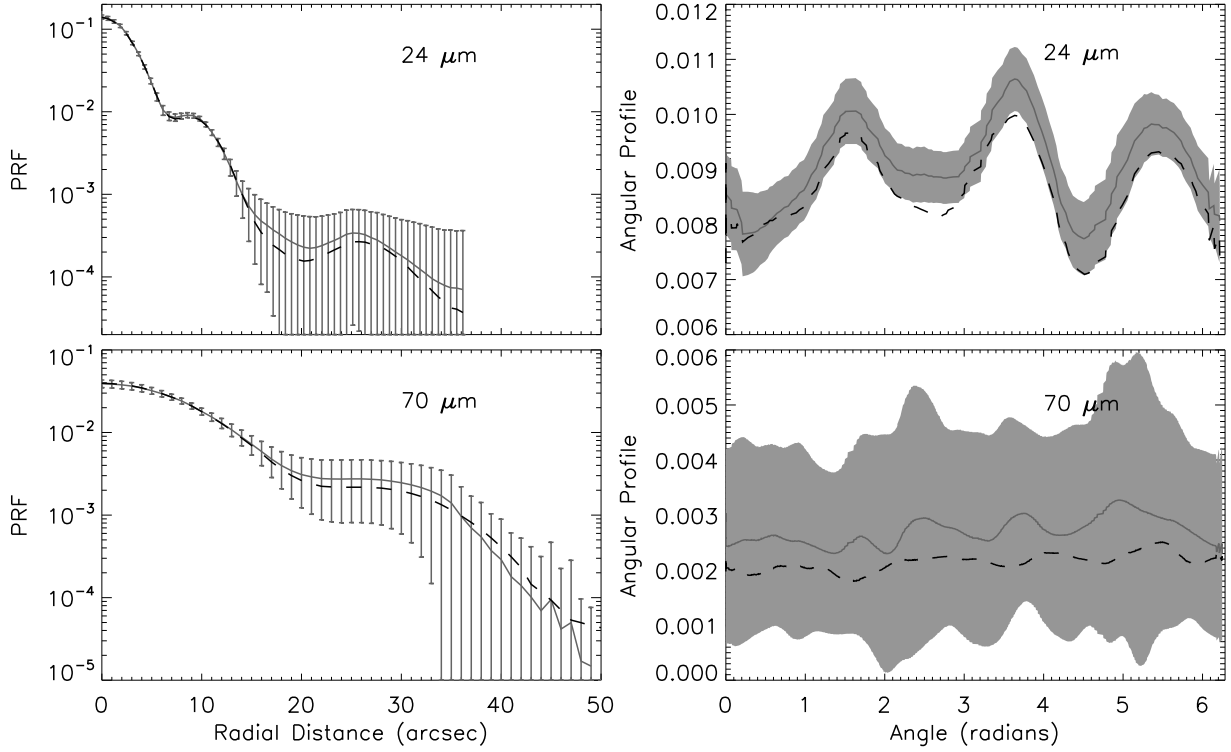


Fig. 8.— Point response functions (PRFs) derived from the SEP *Spitzer* data, as described in §4.3. The left panels show the radially averaged PRFs at $24\ \mu\text{m}$ (top) and $70\ \mu\text{m}$ (bottom). The gray solid curves are the PRFs estimated from our data using the APEX PRF Estimate pipeline, where the error bars represent the standard deviation on these measurements. The dashed black curves are the radially averaged PRFs provided by the SSC. The right panels show the angular profiles of the PRFs at the first Airy ring. The solid gray curves and gray shaded regions are the PRF estimates from the SEP data and the standard deviation on these measurements, respectively, while the dashed black curves are from the PRFs provided by the SSC.

4.5. False Detection Rate

The SNR derived from the data uncertainties does not represent the formal statistical significance of a detection under the assumption of Gaussian distributed noise. Therefore, we estimate the expected fraction of sources in our point-source catalogs that are false detections (i.e. positive noise peaks) through simulation by running the same source-extraction algorithms described in §4.1 and §4.2 on our jackknifed noise realizations for the $24\ \mu\text{m}$ (§3.1) and $70\ \mu\text{m}$ (§3.2) maps. For the $24\ \mu\text{m}$ catalog, we expect 1.8% (~ 1700) of the sources listed in Table 1 to be false detections. For the $70\ \mu\text{m}$ catalog, we expect 1.1% (~ 9 to 10) of the sources listed in Table 3 to be false detections. Note, however, that due to the small number of sources detected in the $70\ \mu\text{m}$ jackknife map, this estimate is crude. Furthermore, for pixels with low coverage (i.e. where there is a small number of BCDs available for averaging), our jackknifing technique is less effective at removing the contribution from real sources. This can leave more pixels with excess positive or negative outliers than would be expected from pure noise, as can be seen by comparing the pixel flux distributions from the jackknifed maps to the simulated noise maps in Figures 2 and 5. For this reason, the false detection rates reported here should be considered upper limits.

4.6. Completeness

We estimate the $24\ \mu\text{m}$ catalog completeness through simulation by injecting point sources with known flux density into the mosaic map and computing their recovery rate. We simultaneously inject 10 000 simulated sources into the $24\ \mu\text{m}$ mosaic map at discrete flux density values ranging from $10\ \mu\text{Jy}$ to $1200\ \mu\text{Jy}$. Since the number density of simulated sources inserted at the same time is low, they do not appreciably change the noise properties of the map. At the same time, by inserting simulated sources into the real map, we account for the effects of confusion noise on the catalog completeness. To avoid contamination from the blending of ≥ 2 sources, every simulated source is injected $> 7.7''$ (~ 2.5 times the half-width at half maximum, HWHM) from any real source and from any other simulated source. We run the same source-extraction algorithm described in §4.1 on these simulated maps; if an input source is detected with $\text{SNR} \geq 5$ within $7.4''$ of its input position, it is considered to be recovered. The $24\ \mu\text{m}$ catalog completeness as a function of intrinsic flux density is shown in Figure 9. The catalog is 80% complete at $230\ \mu\text{Jy}$, and 95% complete at $350\ \mu\text{Jy}$.

We estimate the $70\ \mu\text{m}$ catalog completeness in the same manner. For flux densities ranging from $0.5\ \text{mJy}$ to $25\ \text{mJy}$, we simultaneously inject 10 000 simulated sources into the mosaic map. Every simulated source is injected $> 23''$ (~ 2.5 times the HWHM) from any

real $70\ \mu\text{m}$ source and from other simulated sources. We run the source-extraction algorithm described in §4.2 on these simulated maps, and consider an input source recovered if it is detected with $\text{SNR} \geq 6$ within $20''$ of its input position. The $70\ \mu\text{m}$ catalog completeness is shown in Figure 9. The catalog is 80% complete at 11 mJy, and 95% complete at 15 mJy.

4.7. Aperture Photometry

We use APEX to perform aperture photometry on the sources in this field in order to determine more accurate flux measurements for sources that are not well fit by the PRF and to aid in identifying extended sources. For the $24\ \mu\text{m}$ sources, we use three different circular apertures with radii of $4.9''$, $7.4''$, and $15''$ (1.7, 2.5, and 5.0 times the HWHM of the $24\ \mu\text{m}$ beam, respectively). For each source we estimate the background by computing the mode within an annulus of $20 - 32''$ surrounding the source, and we subtract this background from the aperture fluxes. The aperture photometry for the $24\ \mu\text{m}$ point sources is listed in columns 7 – 9 of Table 1. The uncertainties on the aperture fluxes represent the quadrature sum of the data uncertainties over the aperture area. For sources in the table without aperture measurements, the measured aperture fluxes were $< 0\ \mu\text{Jy}$; such cases typically arise when there is a brighter source located in the background annulus.

For the $70\ \mu\text{m}$ point sources, we use three circular apertures with radii of $16''$, $28''$, and $36''$ (1.8, 3.1, and 4.0 times the HWHM of the $70\ \mu\text{m}$ beam, respectively). We estimate and subtract the background, computed as the mode within an annulus of $60 - 80''$ surrounding the source. The aperture photometry for each $70\ \mu\text{m}$ point source is listed in columns 7 – 9 of Table 3.

We estimate aperture corrections in two ways: 1) by comparing the PRF-fitted flux densities of the point sources to the aperture photometry measurements; and 2) by simulating point sources and comparing the measured aperture fluxes to the known input fluxes. For the first estimate, we consider only sources that are well fit by the PRF ($\chi_r^2 \leq 3$) and have PRF-fitted flux densities $\geq 500\ \mu\text{Jy}$ at $24\ \mu\text{m}$ and $\geq 19\ \text{mJy}$ at $70\ \mu\text{m}$. These latter constraints limit the analysis to sources whose measured fluxes are not on average biased high by noise peaks; this was determined by comparing the input to output fluxes of the simulated sources described in §4.6. The mode of the distribution in the measured aperture to PRF-fitted flux densities for the $24\ \mu\text{m}$ sources is $S_{\text{aper},24}/S_{\text{PRF},24} = 0.53 \pm 0.02$, 0.67 ± 0.07 , and 0.93 ± 0.26 for the $4.9''$, $7.4''$, and $15''$ radius apertures, respectively. For the $70\ \mu\text{m}$ sources, the measured flux ratios from this estimate are $S_{\text{aper},70}/S_{\text{PRF},70} = 0.64 \pm 0.04$, 0.85 ± 0.17 , and 0.97 ± 0.27 for the $16''$, $28''$, and $36''$ radius apertures, respectively.

We next turn to simulations as an alternative estimate of the aperture corrections. We use the same simulations described in §4.6, limited to where the input source flux is $\geq 500 \mu\text{Jy}$ at $24 \mu\text{m}$ and $\geq 19 \text{mJy}$ at $70 \mu\text{m}$. The mode of the distribution in the measured aperture to input flux for the simulated $24 \mu\text{m}$ point sources is $S_{\text{aper},24}/S_{\text{in},24} = 0.52 \pm 0.04$, 0.66 ± 0.08 , and 0.91 ± 0.27 for the $4.9''$, $7.4''$, and $15''$ radius apertures, respectively; for the $70 \mu\text{m}$ simulated sources, they are $S_{\text{aper},70}/S_{\text{in},70} = 0.63 \pm 0.15$, 0.85 ± 0.36 , and 1.00 ± 0.56 for the $16''$, $28''$, and $36''$ radius apertures, respectively. These estimates are in good agreement with those derived from the real point sources. Although the scatter in $S_{\text{aper}}/S_{\text{in}}$ is generally larger (especially for the $70 \mu\text{m}$ data), we adopt the aperture corrections determined from these simulated data, since here we are able to compare the measured aperture fluxes directly to the known intrinsic fluxes. These correction factors are listed in Table 4 for easy reference.

Given that some regions of this field are crowded (mostly at $24 \mu\text{m}$), which can affect both the aperture and background measurements, we recommend using the PRF-fitted flux densities for point sources that are well fit by the PRF. In other cases, it is generally a good idea to visually inspect the region surrounding the source of interest to decide which aperture is best to use, or to recalculate the flux using a different aperture and background annulus if needed.

4.8. Extended Sources

A significant fraction of false detections come from extended sources being split into multiple pixel clusters during image segmentation. As an example, we show the 24 and $70 \mu\text{m}$ postage stamp images centered on the galaxy ESO 158-G 007 in the bottom panels of Figure 7; the small circles and boxes indicate the “sources” initially identified by APEX, where the boxes represent those arising from the extended emission of ESO 158-G 007. We visually inspect the 24 and $70 \mu\text{m}$ images and exclude such false detections from the point-source catalogs.

For a more rigorous analysis, we identify candidate extended sources by comparing the PRF-fitted fluxes to the aperture fluxes, using the $7.4''$ and $16''$ radius apertures for the 24 and $70 \mu\text{m}$ fluxes, respectively. If the PRF-fitted and (corrected) aperture fluxes do not agree within their 3σ uncertainties and the aperture flux is higher, the source is possibly extended. For sources that are well fit by the PRF ($\chi_r^2 \leq 3$), this is true for only 1.7% (2.4%) of the $24 \mu\text{m}$ ($70 \mu\text{m}$) sources and largely arises from multiple sources lying within the aperture radius. For sources with $\chi_r^2 > 3$, 34% (32%) of the $24 \mu\text{m}$ ($70 \mu\text{m}$) sources meet this criterion. Therefore we believe that this criterion will select most of the resolved galaxies in this field.

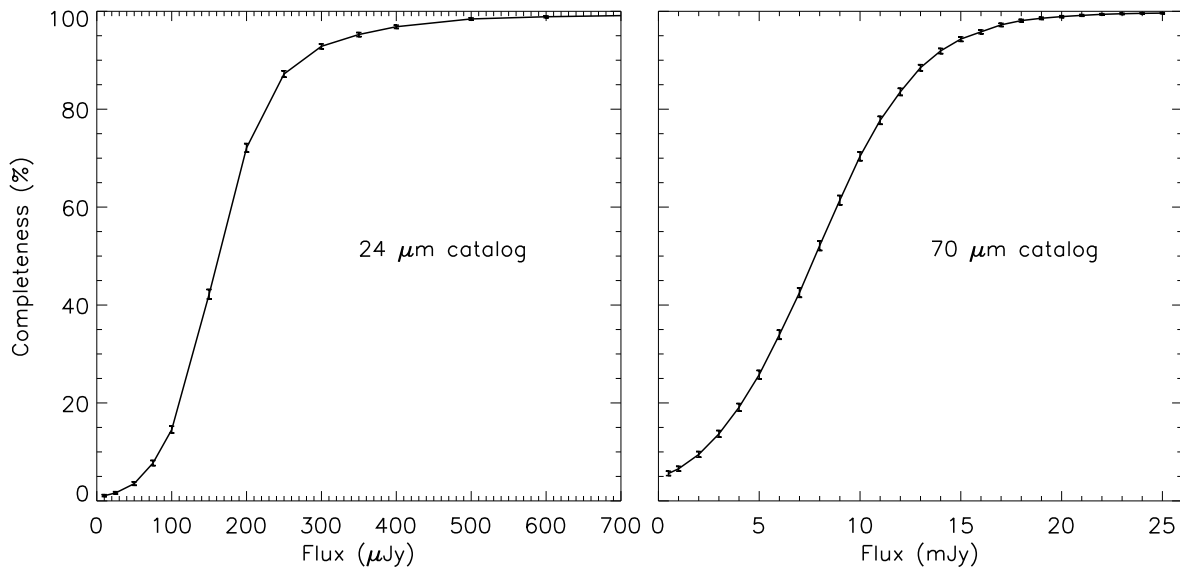


Fig. 9.— The catalog completeness for the $24\ \mu\text{m}$ (left) and $70\ \mu\text{m}$ (right) catalogs. The error bars represent the 95% confidence interval from the binomial distribution.

Table 4. Aperture Corrections

	Aperture Radius "	Aperture Correction
$24\ \mu\text{m}$	4.9	1.92
	7.4	1.52
	15	1.10
$70\ \mu\text{m}$	16	1.59
	28	1.18
	36	1.00

Note. — To correct the measured aperture fluxes listed in Tables 1 and 3, multiply by the values in this table.

At $24\ \mu\text{m}$ there are a total of 758 candidate extended sources with $\chi_r^2 > 3$. We also consider an additional 604 point sources that are well fit by the PRF, but whose PRF-fitted and aperture fluxes differ by more than 3σ ; these sources are often found in proximity to each other and could potentially arise from extended emission from a single source. We cross-check the positions of these sources with the NASA Extragalactic Database (NED). For those with an extragalactic counterpart, we visually compare the optical/near-IR images and the $24\ \mu\text{m}$ emission in order to select an appropriate aperture size for measuring the $24\ \mu\text{m}$ surface brightness. If the emission is contained within a $15''$ aperture, we do not remeasure the aperture photometry since this information is already given in Column 9 of Table 1. For the 63 extended sources that require apertures with radii $> 15''$, we first use the APEX QA pipeline to subtract the 93 098 point sources from the $24\ \mu\text{m}$ mosaic; we then carry out aperture photometry on this residual map for each extended source using the appropriate aperture sizes and source positions from NED. This is demonstrated for ESO 158-G 007 in the bottom panels of Figure 7, where the black cross marks the source position from NED, and the black dashed circle indicates the aperture radius ($60''$) used. The resolved galaxy catalog is given in Table 2. According to the MIPS Instrument Handbook, the total uncertainty on the flux calibration for extended sources is $\sim 15\%$.

We carry out an independent check for candidate extended sources with the $70\ \mu\text{m}$ catalog using the same criterion. There are 16 sources for which the measured aperture flux is larger than PRF-fitted flux and discrepant by $> 3\sigma$. To this list, we add an additional six sources that do not meet this criterion, but by eye are clearly extended. For sources with an extragalactic counterpart found in NED, we pick out 8 extended sources that require apertures larger than $36''$ (i.e. the largest aperture radius used on the point-source catalog). As with the $24\ \mu\text{m}$ data we carry out aperture photometry for these extended sources after subtracting the 891 $70\ \mu\text{m}$ point sources from the map. These measurements are listed in column 5 of Table 2. For the remaining extended $24\ \mu\text{m}$ sources, we list in Table 2 the $70\ \mu\text{m}$ PRF-fitted fluxes and uncertainties from the point-source catalog where available (Table 3), and we note the $70\ \mu\text{m}$ source identification in the last column.

5. Conclusions

We have imaged an $11.5\ \text{deg}^2$ field towards the SEP at 24 and $70\ \mu\text{m}$ with MIPS, achieving 1σ depths of $31 - 110\ \mu\text{Jy beam}^{-1}$ at $24\ \mu\text{m}$ and $2.2 - 40\ \text{mJy beam}^{-1}$ at $70\ \mu\text{m}$. We identify 93 098 point sources with $\text{SNR} \geq 5$ at $24\ \mu\text{m}$, and 63 resolved galaxies. Through simulations, we determine that the $24\ \mu\text{m}$ point-source catalog has an expected false detection rate of 1.8% , and is 80% complete at $230\ \mu\text{Jy}$. From the $70\ \mu\text{m}$ map, we identify 891

point sources with $\text{SNR} \geq 6$; this $70\ \mu\text{m}$ catalog is 80% complete at 11 mJy, with a false detection rate of 1.1%.

We will make the 24 and $70\ \mu\text{m}$ mosaic images, their corresponding uncertainty and coverage maps, and the catalogs described in this paper available to the public through the NASA/IPAC Infrared Science Archive (IRSA)⁷ as a *Spitzer* contributed data-set.

This work is based on observations made with the *Spitzer* Space Telescope, which is operated by the Jet Propulsion Laboratory, California Institute of Technology under a contract with NASA. Support for this work was provided by NASA through an award issued by JPL/Caltech. This research was supported by the Natural Sciences and Engineering Research Council of Canada and by the Canadian Space Agency. This research has made use of the NASA/IPAC Infrared Science Archive (IRSA) and the NASA/IPAC Extragalactic Database (NED), both of which are operated by the Jet Propulsion Laboratory, California Institute of Technology, under contract with the National Aeronautics and Space Administration.

Facilities: *Spitzer* (MIPS)

REFERENCES

- Aretxaga, I., et al. 2007, MNRAS, 379, 1571
- Ashby, M. L. N., et al. 2006, ApJ, 644, 778
- Austermann, J. E., et al. 2010, MNRAS, 401, 160
- Bertoldi, F., et al. 2007, ApJS, 172, 132
- Blain, A. W., Smail, I., Ivison, R. J., Kneib, J., & Frayer, D. T. 2002, Phys. Rep., 369, 111
- Borys, C., Chapman, S., Halpern, M., & Scott, D. 2003, MNRAS, 344, 385
- Chapin, E. L., et al. 2009, MNRAS, 398, 1793
- . 2010, ArXiv e-prints
- Chapman, S. C., Blain, A. W., Smail, I., & Ivison, R. J. 2005, ApJ, 622, 772

⁷<http://irsa.ipac.caltech.edu/>

- Coppin, K., et al. 2006, MNRAS, 372, 1621
- Devlin, M. J., et al. 2009, Nature, 458, 737
- Dye, S., et al. 2008, MNRAS, 386, 1107
- . 2009, ApJ, 703, 285
- Engelbracht, C. W., et al. 2007, PASP, 119, 994
- Fixsen, D. J., Dwek, E., Mather, J. C., Bennett, C. L., & Shafer, R. A. 1998, ApJ, 508, 123
- Frayer, D. T., et al. 2006a, AJ, 131, 250
- . 2006b, ApJ, 647, L9
- . 2009, AJ, 138, 1261
- Gordon, K. D., et al. 2005, PASP, 117, 503
- . 2007, PASP, 119, 1019
- Greve, T. R., Ivison, R. J., Bertoldi, F., Stevens, J. A., Dunlop, J. S., Lutz, D., & Carilli, C. L. 2004, MNRAS, 354, 779
- Greve, T. R., Pope, A., Scott, D., Ivison, R. J., Borys, C., Conselice, C. J., & Bertoldi, F. 2008, MNRAS, 389, 1489
- Hainline, L. J., Blain, A. W., Smail, I., Frayer, D. T., Chapman, S. C., Ivison, R. J., & Alexander, D. M. 2009, ApJ, 699, 1610
- Hauser, M. G., et al. 1998, ApJ, 508, 25
- Laurent, G. T., et al. 2005, ApJ, 623, 742
- Marsden, G., et al. 2009, ApJ, 707, 1729
- Masci, F. J., Laher, R., Fang, F., Fowler, J. W., Lee, W., Stolovy, S., Padgett, D., & Moshir, M. 2005, in *Astronomical Society of the Pacific Conference Series*, Vol. 347, *Astronomical Data Analysis Software and Systems XIV*, ed. P. Shopbell, M. Britton, & R. Ebert, 468–+
- Matsuhara, H., et al. 2006, PASJ, 58, 673
- Papovich, C., et al. 2004, ApJS, 154, 70

Pascale, E., et al. 2008, *ApJ*, 681, 400

—. 2009, *ApJ*, 707, 1740

Perera, T. A., et al. 2008, *MNRAS*, 391, 1227

Pope, A., et al. 2006, *MNRAS*, 370, 1185

Puget, J., Abergel, A., Bernard, J., Boulanger, F., Burton, W. B., Desert, F., & Hartmann, D. 1996, *A&A*, 308, L5+

Rieke, G. H., et al. 2004, *ApJS*, 154, 25

Sanders, D. B., et al. 2007, *ApJS*, 172, 86

Scott, K. S., et al. 2008, *MNRAS*, 385, 2225

—. 2010, *MNRAS*, 684

Scott, S. E., et al. 2002, *MNRAS*, 331, 817

Wang, W.-H., Cowie, L. L., & Barger, A. J. 2006, *ApJ*, 647, 74

Weiß, A., et al. 2009, *ApJ*, 707, 1201